Comparison of Fourier optics-based methods for modelling coherence scanning interferometry

Helia Hooshmand*[a], Tobias Pahl[b], Peter J. de Groot[c], Peter Lehmann[b], Athanasios Pappas[a], Rong Su[d], Richard Leach[a], Samanta Piano[a]

[a]University of Nottingham, Nottingham, UK
[b]Measurement Technology Group, University of Kassel, Kassel, Germany
[c]Zygo Corporation, Middlefield, CT USA
[d]Shanghai Institute of Optics and Fine Mechanics, Shanghai, China

Abstract. Coherence scanning interferometry (CSI) is a widely used optical method for surface topography measurement of industrial and biomedical surfaces. The operation of CSI can be modelled using approximate physics-based approaches with minimal computational effort. A critical aspect of CSI modelling is defining the transfer function for the imaging properties of the instrument in order to predict the interference fringes from which topography information is extracted. Approximate methods, for example, elementary Fourier optics, universal Fourier optics and foil models, use scalar diffraction theory and the imaging properties of the optical system to model CSI surface topography measurement. In this paper, the simulated topographies of different surfaces, including various sinusoids, two posts and a step height, calculated using the three example methods are compared. The presented results illustrate the agreement between the three example models.

Keywords: Surface topography, CSI, scattering, transfer function

*Helia.Hooshmand@nottingham.ac.uk; https://www.nottingham.ac.uk/research/manufacturing-metrology

1 Introduction

Interference microscopy, particularly coherence scanning interferometry (CSI)[1], is a popular optical technique for high-precision surface topography measurement[2, 3]. The broad range of CSI applications, from high-precision measurements of semiconductor devices to quality control in industrial manufacturing, has motivated the development of physics-based models to predict interference signals and analyse measurement results[4-7]. The development of these models addresses the practical need for a better understanding of the instrument characteristics and performance specifications, optimisation of instrument configurations for good practice, and uncertainty estimation using virtual instruments.

Modelling of CSI for the full range of current and future applications of these instruments is a complex task, which can be addressed by approximate physics-based models that simplify three-dimensional (3D) optical imaging using the linear theory of imaging[8, 9] and well-established scattering approximations[10-12]. A number of practical, approximate models have been developed with known limitations in their validity ranges[11, 13], including the neglect of near-field and polarisation effects, multiple scattering and surface films[14]. These approximate models serve a useful purpose constrained by the fundamental limits of scalar diffraction and linear imaging theory[15, 16].

Using approximate models, the formation of interference fringes can be considered as a linear filtering operation characterised by a transfer function (TF) in the spatial frequency domain. Linear systems theory has been extensively applied to 2D optical imaging[10]. The linear systems theory approach to interferometric imaging allows in many cases for the compensation of measurement errors by the application of an inverse filter[17]. Furthermore, approximate models are easier to implement than more rigorous solvers of Maxwell's equations, are computationally efficient and can provide insight into fundamental sources of measurement error related to light scattering and imaging[18].

Elementary Fourier optics (EFO)[19, 20], universal Fourier optics (UFO)[21, 22] and the foil model[16, 23] benefit from scalar approximation methods that consider the imaging properties of the optical system. These models assume that local surface curvatures are small enough to comply with Kirchhoff's approximation[11]; however, each method uses a different approach to model the surface and the TF. EFO models the surface as a phase object together with classical Fourier optics methods and a 2D partially coherent optical TF. EFO methods, along with a 2D

representation of the propagating light field, have been used to model an interference microscope[19, 24] and to predict the linear instrument TF and residual nonlinear measurement errors for optical measurements of surface topography[25]. The UFO method also uses the phase object approximation and a 2D TF, where the 2D TF equals the horizontal cross-section of a 3D TF[21]. In the foil model, the surface is defined as a 3D thin foil-like object, and the 3D TF maps this surface to the interference fringes[16]. The foil model has been used in various surface topography measurement applications including signal modelling[16, 26], calibration and adjustment of the 3D TF[27] and lens aberration compensation[28] in a CSI instrument. Applications of the foil model are not limited to interference microscopy but can also be extended to 3D image formation in focus variation microscopy[29].

While the mathematical derivations in the literature for the EFO, UFO and foil models differ from each other, we shall show here that they predict the same measurement results within their respective validity regimes. To demonstrate the comparability of the EFO, UFO and foil models, we perform numerical calculations based on simulated object profiles that include sinusoids, step heights and closely-space rectangular surface features, for different instrument configurations, such as numerical aperture (NA) and light source spectrum. Some primary results have been presented previously[30]. These results demonstrate the consistency of these approximate methods based on similar scattering and imaging theories and improve confidence in approximate methods as a foundation for the development of virtual CSI instruments.

2 EFO, UFO and Foil models

The EFO, UFO and foil models are well-established approximate models. Detailed descriptions of the background theory and applications of these models are available elsewhere[16, 19-21, 23, 25, 31]. In all three models, imaging of the surface topography is described as a linear filtering process characterised by a TF. In the following sections, we briefly describe how the TF, object and image are simulated in each model.

2. 1. EFO

In the EFO model, the contribution of surface topography in interference microscopy modelling is approximated by introducing a phase shift proportional to the surface heights $z = h_o(x)$ to the object light field (i.e. the light field immediately after reflection). Assuming uniform monochromatic illumination and surface reflectivity, the 2D object field is approximated as [19]

$$U_o(\mathrm{x}) = exp[-i2\pi K h_o(x)], \tag{1}$$

where $K = 2/\lambda\Omega$ is the interference fringe frequency, λ is the wavelength of the incident light and Ω is the obliquity factor that approximates the effect of the illumination geometry by integrating over all incident angles. This approximation is a significant simplification compared to pupil integration methods[32], including 3D TF models that calculate the contribution of each incident wave vector within the pupil plane independently[33]. This simplification enables a classical 2D Fourier optics analysis, at the expense of disregarding focus effects on surfaces with large height variations. The image field is obtained by applying a filtering operation in the spatial frequency domain using a 2D partially-coherent TF (PCTF): [10]

$$\tilde{U}_s(k_x) = \tilde{O}(k_x)\tilde{U}_o(k_x), \tag{2}$$

where k_x is the projection of the scattered wave vector in the pupil plane, $\tilde{U}_s(k_x)$ and $\tilde{U}_o(k_x)$ are the Fourier transforms or plane wave spectra of the image and object fields respectively, and $\tilde{O}(k_x)$ is the PCTF. As an example, for an interference microscope with Köhler illumination and a filled illumination pupil of the same size as the imaging pupil, the PCTF is similar in form to the modulation TF for conventional imaging:

$$\tilde{O}(k_x) = \frac{2}{\pi}\left[\cos^{-1}\left(\frac{|k_x|}{k_{\max}}\right) - \left(\frac{|k_x|}{k_{\max}}\right)\sqrt{1-\left(\frac{|k_x|}{k_{\max}}\right)^2}\right]\mathrm{rect}\left[\frac{k_x}{2k_{\max}}\right], \tag{3}$$

where $k_{\max} = 2A_N/\lambda$ and A_N is the value of the NA. The scattered field in the image plane $U_s(x)$ is given by the inverse Fourier transform of $\tilde{U}_s(k_x)$. For a broadband source, Eqs. (1) to (3) are repeated to give $U_s(x,K)$. Although it is possible to simulate the interference fringes in the EFO model (inverse Fourier transform of $U_s(x,K)$ along *z*-axis), surface topography can be calculated directly from the image field[19, 20]. The limits of applicability for EFO modelling are reported elsewhere[20].

2. 2. UFO

In the UFO model, the optical field $U_o(x,y)$ on a surface $h_o(x,y)$ immediately after reflection is given by

$$U_o(x,y,K_z) = \exp\left[-2\pi i K_z h_o(x,y)\right], \tag{4}$$

where K_z is the component of **K** along the *z*-axis, where[21, 31]

$$\mathbf{K} = \mathbf{k_s} - \mathbf{k_i} = \begin{pmatrix} K_\rho \\ K_z \end{pmatrix} = k_0 \begin{pmatrix} |\sin(\theta_s) - \sin(\theta_i)| \\ \cos(\theta_s) + \cos(\theta_i) \end{pmatrix}. \quad (5)$$

In Eq. (5), $\mathbf{k_s}$ and $\mathbf{k_i}$ are the scattered and incident wave vectors characterised by scattered and incident angles θ_s and θ_i in relation to the *z*-axis respectively, and $k_0 = 1/\lambda$ is the wave-number. Unlike the EFO model, the effect of multiple illumination incident angles and orientations is included in the UFO method, to account for focus effects.

The interference intensity between the object and the reference field in the **K**-space results from frequency domain filtering of the Fourier representation of the object field $\tilde{U}_o(\mathbf{K})$ as[34]

$$\tilde{I}(\mathbf{K}) \sim \tilde{U}_0(\mathbf{K})\tilde{H}(\mathbf{K}). \quad (6)$$

In Eq. (6), $\tilde{H}(\mathbf{K})$ is the 3D optical TF of the imaging system. An analytical form for the 3D TF follows from the 3D correlation of the spherical caps corresponding to the incident and scattered wave vectors[35, 36]. It has been shown that the shape of the 3D TF of a diffraction-limited interference microscope with uniform monochromatic pupil illumination depends on the surface under investigation[31, 35]. For piecewise continuous surfaces, the normalised 3D TF for monochromatic light of wavenumber k_0 results in[34]

$$\tilde{H}(K_\rho,K_z,k_0)=\begin{cases}\dfrac{K_z}{2k_0} & \text{for } K_{z,0}\le K_z\le K_{z,\max},\\ \left[1-\dfrac{2}{\pi}\cos^{-1}\left(\dfrac{|\mathbf{K}|\left(K_z-K_{z,\min}\right)}{K_\rho\sqrt{4k_0^2-|\mathbf{K}|^2}}\right)\right]\dfrac{K_z}{2k_0} & \text{for } K_{z,\min}\le K_z\le K_{z,0},\\ 0 & \text{elsewhere,}\end{cases} \tag{7}$$

where $K_{z,\min}$, $K_{z,0}$ and $K_{z,\max}$ are given by

$$\begin{aligned} K_{z,\min} &= 2k_0\sqrt{1-A_N{}^2},\\ K_{z,0} &= k_0\sqrt{1-A_N{}^2}+k_0\sqrt{1-\left(\frac{K_\rho}{k_0}-A_N\right)^2},\\ K_{z,\max} &= 2k_0\sqrt{1-\frac{K_\rho^2}{4k_0^2}}. \end{aligned} \tag{8}$$

To consider polychromatic light, the individual monochromatic 3D TFs are superimposed after weighting to account for the spectral distribution.

2. 3. Foil model

Consider a monochromatic plane wave $U_i(\mathbf{r})=exp(2\pi i\mathbf{k_i}.\mathbf{r})$ propagated with a 3D wave vector $\mathbf{k_i}$ illuminating a 3D scattering object with a surface height function of $h_o(x,y)$. Using the integral theorem of Helmholtz and Kirchhoff, the scattered field can be expressed as a surface integral[13]. Applying Kirchhoff's boundary conditions[11] and the free-space Green's function into the integral, the scattered far-field can be written as[16]

$$\tilde{U}_s(\mathbf{K}+\mathbf{k_i}) = -\frac{1}{2k_0}\delta(|\mathbf{K}+\mathbf{k_i}|-k_0)\left[\frac{|\mathbf{K}|^2}{\mathbf{K}.\mathbf{z}}\right]\iiint R\,\delta\left[z-h_o(x,y)\right]exp(-2\pi i\mathbf{K}.\mathbf{r})d^3\mathbf{r}, \quad (9)$$

where $\mathbf{K} = \mathbf{k_s} - \mathbf{k_i}$, $\mathbf{k_s}$ is the scattering wave vector, $k_0 = 1/\lambda$ is the wavenumber and R is the amplitude reflection coefficient. The term $R\,\delta\left[z-h_o(x,y)\right]$ is proportional to what is referred to as the "foil model" of the surface[16]. It is noteworthy that the Fourier transform of the foil representation of a surface, expressed by a 1D Dirac delta function follows the surface height with respect to the *z*-coordinate, resulting in the phase object representation of the electric field shown in Eq. (4) as follows

$$\int_{-\infty}^{+\infty}\delta\left[z-h_o(x,y)\right]exp(-2\pi iK_z z)dz = exp[-2\pi iK_z h_o(x,y)]. \quad (10)$$

Therefore, the phase object presented in the UFO model and the surface foil described in the foil model both offer an equivalent approach to modeling the object.

In interference microscopy, the scattered field over the surface is obtained by a 3D surface TF (STF) of a microscope objective with a finite NA and a pupil apodisation function of $P(\mathbf{k})$. The STF with regards to the incident wave vector $\mathbf{k_i}$ is a truncated spherical shell expressed by[16, 23]

$$\tilde{G}_{\mathrm{NA}}(\mathbf{K}+\mathbf{k_i}) \propto P^2(\mathbf{K}+\mathbf{k_i})\delta(|\mathbf{K}+\mathbf{k_i}|-k_0)\mathrm{step}\left[\frac{(\mathbf{K}+\mathbf{k_i}).\mathbf{z}}{k_0}-\sqrt{1-A_N{}^2}\right]. \quad (11)$$

For an ideal aplanatic case $P(\mathbf{K}+\mathbf{k_i}) = \left[(\mathbf{K}+\mathbf{k_i}).\mathbf{z}/k_0\right]^{1/2}$. Using the definition of the STF and the foil model of the surface, Eq. (9) can be re-written as

$$\tilde{U}_s(\mathbf{K}+\mathbf{k_i}) = \left[\frac{|\mathbf{K}|^2}{2\mathbf{K}.\mathbf{z}}\right]\tilde{F}(\mathbf{K})\tilde{G}_{\mathrm{NA}}(\mathbf{K}+\mathbf{k_i}), \tag{12}$$

where $\tilde{F}(\mathbf{K})$ is the 3D Fourier transform of the foil model of the surface. Using Eq. (12), and considering all possible incident wave vectors, the Fourier transform of the interference term between the incident and scattered field is given by[23]

$$\tilde{I}(\mathbf{K}) = \left[\frac{|\mathbf{K}|^2}{2\mathbf{K}.\mathbf{z}}\right]\tilde{F}(\mathbf{K})\sum_{\mathbf{i}}\tilde{G}_{\mathrm{NA}}(\mathbf{K}+\mathbf{k_i}). \tag{13}$$

This equation represents the product of the 3D Fourier transform of the foil model of the surface and the optical 3D TF according to the foil model considering all possible incident and scattered wavevectors. The interference fringes can be obtained by applying an inverse Fourier transform to Eq. (13).

3 Comparison results for phase measurements

In this section, the simulated TFs and measurement results for the EFO, UFO and foil models are compared for measurements that use interference phase to determine surface profiles. In all simulations, the light source is assumed to have a Gaussian wavenumber spectrum with a mean wavelength of 0.57 μm similar to a common CSI instrument. The interference microscope is configured with Köhler illumination and the objective aperture is fully filled (the illumination pupil is equal to the observation pupil). We also assume that the objective pupil function is consistent with an aplanatic imaging system[33] satisfying Abbe's sine condition.

3. 1 Comparison of the simulated profiles

The detailed specification of the nominal profiles and the optics, including NA, objective, and full-width at half maximum (FWHM) wavelength bandwidth of the light source, considered for simulation are shown in Table 1. For each test, all models share the same lateral resolution, which is embedded within the simulated TF and determined by the NA specific to that particular test.

Table 1. Summary of simulated samples and optics. The mean wavelength equals 0.57 μm for all simulations.

Test	Sample			Optics		
	Type	**Width / µm**	**Height / µm**	**NA**	**Objective**	**FWHM / µm**
Step	Step	8	0.75	0.15	5.5×	0.12
		Period / µm	**Amplitude / µm**			
S1	Sine	40	0.3	0.08	2.75×	0.08
S2	Sine	10	0.15	0.15	5.5×	0.08
S3	Sine	10	0.15	0.3	10×	0.08
S4	Sine	10	0.15	0.55	50×	0.08
S5	Sine	10	0.57	0.7	100×	0.08
		Period / µm	**Amplitude / µm**			
DS	Double sine	10; 160	0.15; 5.0	0.3	10×	0.08
		Centre-to-centre Spacing; Post Width / µm	**Height / µm**			
TP1	Two-posts	1; 0.45	0.05	0.3	10×	0.08
TP2	Two-posts	0.5; 0.2	0.05	0.8	100×	0.08

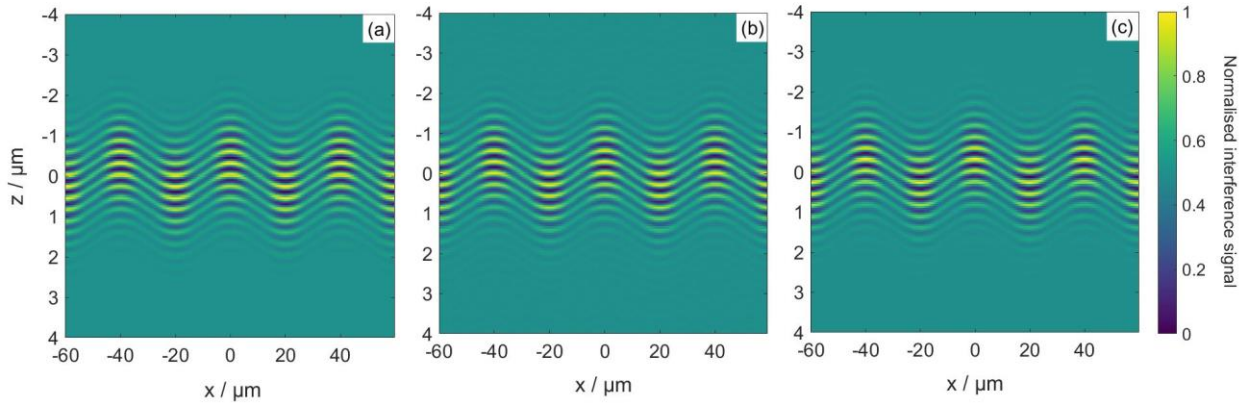

Figure 1. The interference fringe pattern simulated by (a) EFO, (b) UFO and (c) foil corresponding to the S1 test in Table 1.

As a part of CSI modelling, the EFO, UFO and foil models can simulate the interference signal. Figure 1 shows an example of the simulated CSI signal obtained by the (a) EFO, (b) UFO and (c) foil models for the S1 test in Table 1. In interference microscopy, the surface topography can be obtained using an appropriate surface reconstruction method, e.g., envelope detection[37], frequency domain analysis (FDA)[38] and the correlogram correlation method[39]. The FDA-envelope method provides a first estimation of the surface height corresponding to the location of the coherence envelope. This can be achieved by fitting a linear model to the Fourier component phases in the spatial frequency domain. Using FDA-phase, the height value is calculated by interpolating the linear fit at the spatial frequency for which the Fourier magnitude is greatest. In the context of the UFO model, it has been shown that the lateral resolution for interference microscopy can be enhanced by selecting specific Fourier components, rather than using linear phase fitting[34]. However, in this paper, the primary goal is the comparison of different scattering and imaging models, rather than the comparison of reconstruction algorithms. Hence, the

interference signal data generated by the EFO, UFO and foil models are analysed using the same FDA-phase algorithm.

Simulated measurement results obtained by the EFO, UFO and foil models using the configurations shown in Table 1 are illustrated in Figure 2. In Figure 2, a to i show the nominal and reconstructed profiles obtained by the EFO, UFO and foil models along the *x*-axis while a' to i' illustrate the difference between the reconstructed and nominal profiles (that is, the predicted height measurement error) for each modelling method. Finally, the relative signal strength of the interference fringe data for the UFO, EFO and foil models are shown in a" to i". The relative signal strength plot shows the amplitude of the interference signal, normalised to the highest signal in the data set. The fringe signal data for the S1 test in Figure 2 (b") clearly shows that at steep slopes, the signal level (interference fringe contrast) is lower than at the peak and valley positions. Due to the overlapping of the data, the individual curves cannot be distinguished in most of the subplots of Figure 2. The inset of Figure 2 (h) illustrates the differences between the reconstructed profiles, in this case, considered negligibly small. In Figure 2 (a"), at the edges of the step where the signal data are low, the data points corresponding to the relative signal value below the minimum modulation threshold are removed from the reconstructed profile. The so-called batwing effect[40], which appears when discontinuous surfaces with sharp edges (step heights smaller than the coherence length) are measured with CSI, can be seen in Figure 2 (a'). However, since the simulated data are analysed using an FDA-phase algorithm, the batwing effect is not significant[41].

In the S2 to S4 tests (sinusoidal profiles with the same maximum slope angles and minimum curvatures), increasing the NA causes the height error to decrease in all methods. The DS test

with the height range of ± 5.15 μm, demonstrates that the EFO, UFO and foil models are not restricted to small surface heights (e.g., $\leq \lambda/4$). In the TP1 and TP2 tests, post separations are chosen to be close to the Sparrow resolution limit[42] (0.95 μm and 0.43 μm respectively). Figure 2 (h, h', i and i') illustrate that higher NA results in higher lateral resolution and amplitude of the simulated profile in all three models. Additionally, smoothening of peaks in TP1 and TP2 tests is anticipated in a linear process, attributed to the presence of out of pass band diffraction orders.

The comparison of the different simulated profiles obtained by EFO, UFO and foil models shows that there is good agreement between these three approaches. The root-mean-square (RMS) of the difference between the simulated profiles obtained by each two models is within the sub-nanometre range. This confirms that they are based on common physical assumptions, even though they use different approaches to model the surface and TF.

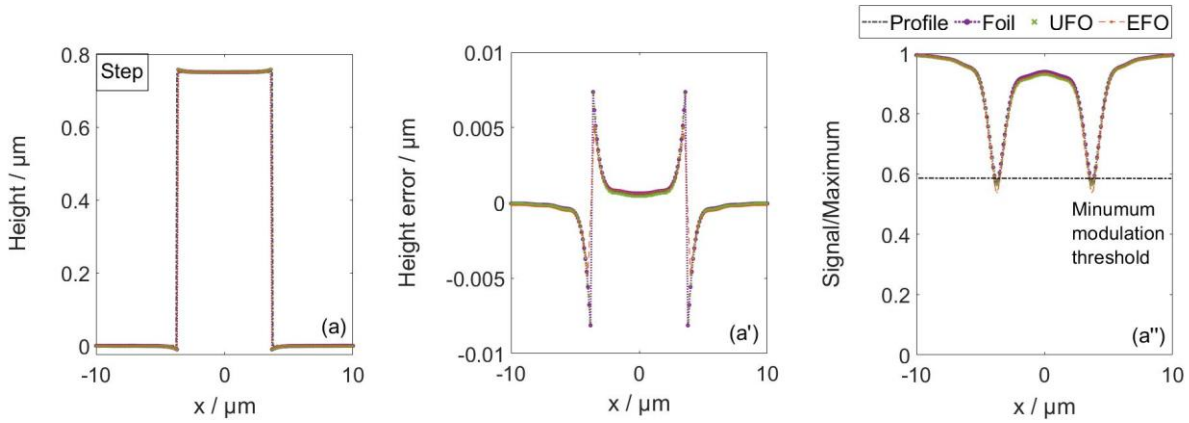

237

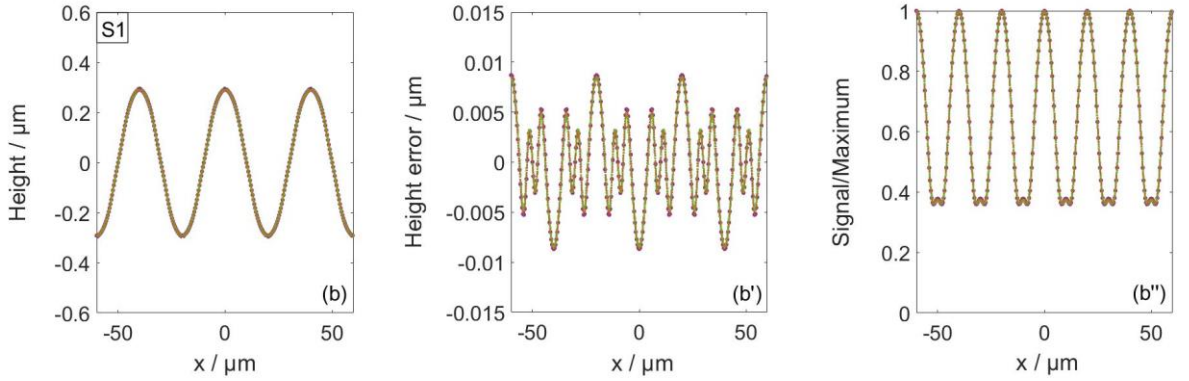

238

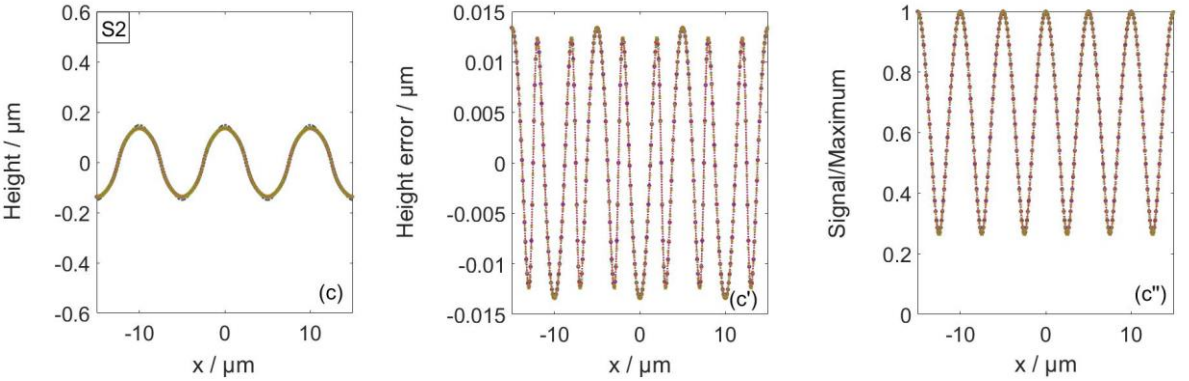

239

240

241

242

243

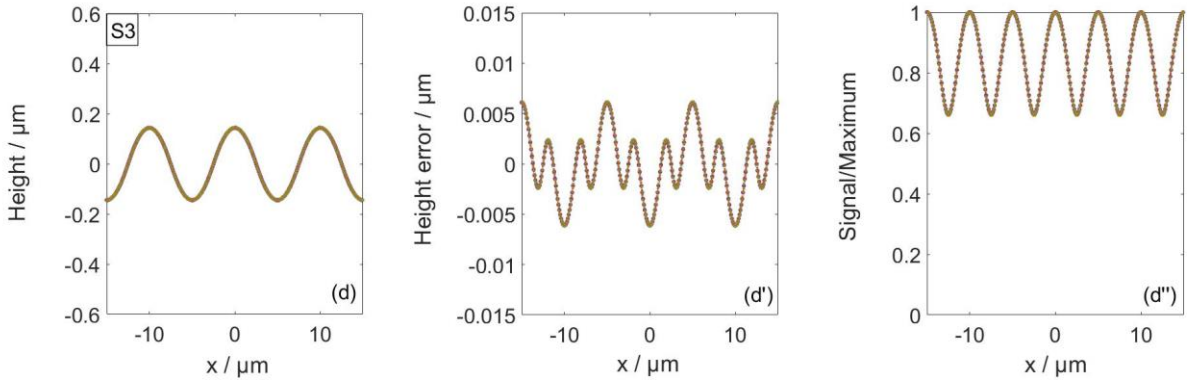
S3
Height / µm
Height error / µm
Signal/Maximum
x / µm
(d)
(d')
(d'')

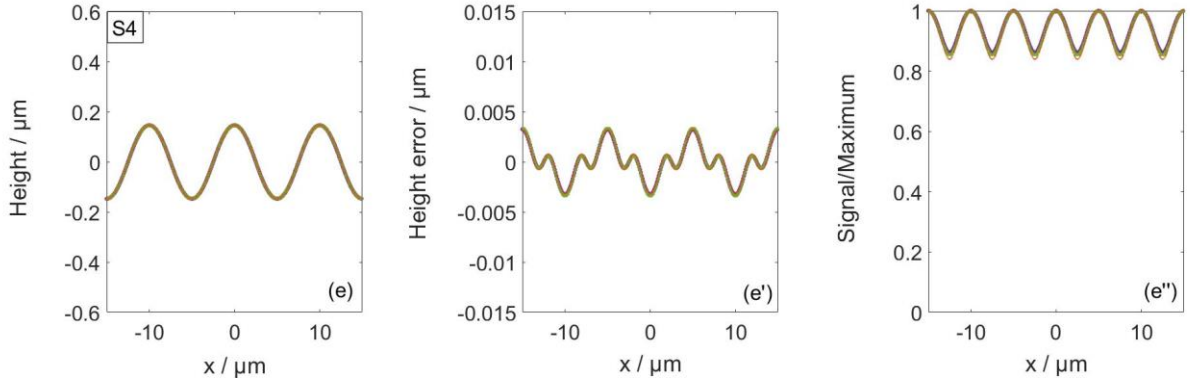
S4
Height / µm
Height error / µm
Signal/Maximum
x / µm
(e)
(e')
(e'')

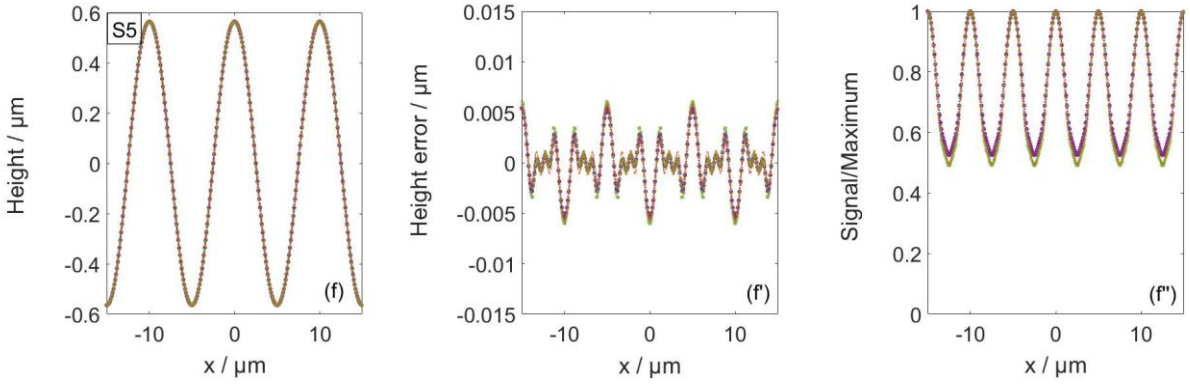
S5
Height / µm
Height error / µm
Signal/Maximum
x / µm
(f)
(f')
(f'')

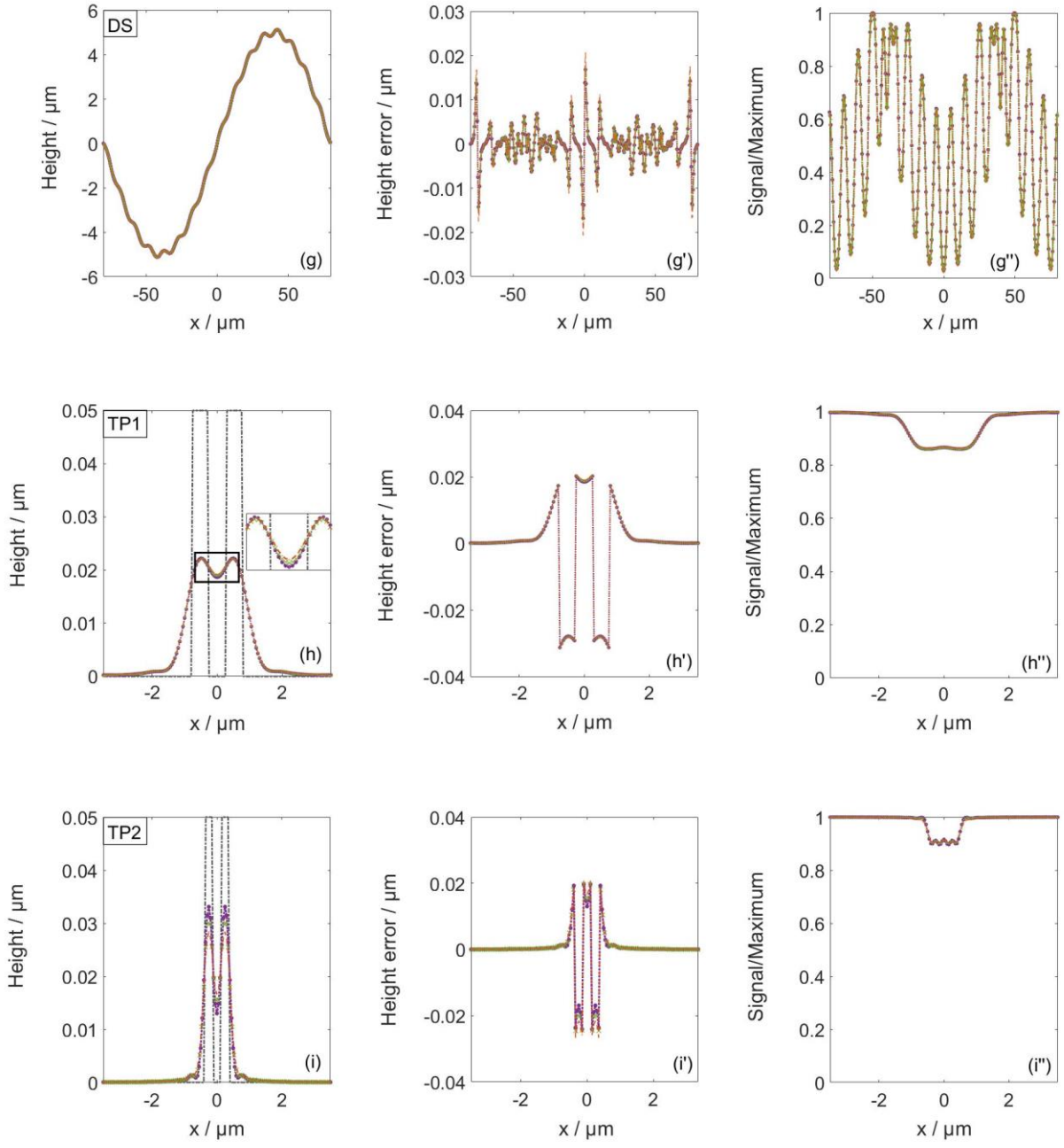

Figure 2. (a to i) Nominal and reconstructed profiles obtained by the EFO, UFO and foil models along the *x*-axis. The specification of the samples and optics used at each row are provided in Table 1. (a' to i') difference between the reconstructed and nominal profiles for EFO, UFO and foil models. (a" to i") relative signal strength of the fringe data in the EFO, UFO and foil models.

4 Comparison of the TFs

In addition to the simulation and comparison of the various profiles for the three models illustrated in Figure 2, a second comparison directly compares the TFs of the EFO, UFO and foil models. Figure 3 shows the *x*,*z*-plane cross-sectional view of the simulated 3D (a to d) foil and (a' to d') UFO TFs that are obtained using the analytical and numerical models respectively, and (a" to d") 2D EFO TF along the *x*-axis. In Figure 2, the behaviour of the TF corresponding to each model is observed for four different NAs of (a to a") 0.8, (b to b") 0.55, (c to c") 0.3 and (d to d") 0.15. It should be noted that all TFs are simulated considering a Gaussian light source with a mean wavelength of 0.57 μm, an FWHM bandwidth of 0.08 μm and a fully filled objective aperture that obeys Abbe's sine condition. Comparing the rows of Figure 3, it is evident that increasing the NA causes the TF to broaden along the *x*-axis. Figure 3 also shows that, despite the small differences between the 3D TFs of the UFO and foil models around the side lobes, they are in general agreement since the simulated profiles obtained by these models are almost identical, as shown in Figure 2. Apart from the numerical calculation of the 3D TF in the foil model and the analytical result according to Eqs. (7) and (8) used in the UFO model, the TFs differ by the factor in square brackets in Eq. (12) used in the foil model. This so-called inclination factor is derived from the Kirchhoff approximation[11] assuming plane wave illumination. In the UFO model, the inclination factor has been adapted to a microscope with Köhler illumination and is considered in the 3D TF according to Eq. (7). Nevertheless, the 3D TFs show slight deviations for larger values of K_x and K_y, especially for high NAs (≥ 0.7). Figure 4 illustrates the subtraction of the magnitude of the normalised 3D TF in the foil model from that in the UFO model for the NAs of (a) 0.8 and (b) 0.3. The average of the RMS of the

difference between the magnitude of the normalised TFs of the UFO and foil models over the range of provided NAs is of the order of 10^{-3}. The 2D TF of the EFO model corresponds to the integration of the 3D TFs along the *z*-axis.

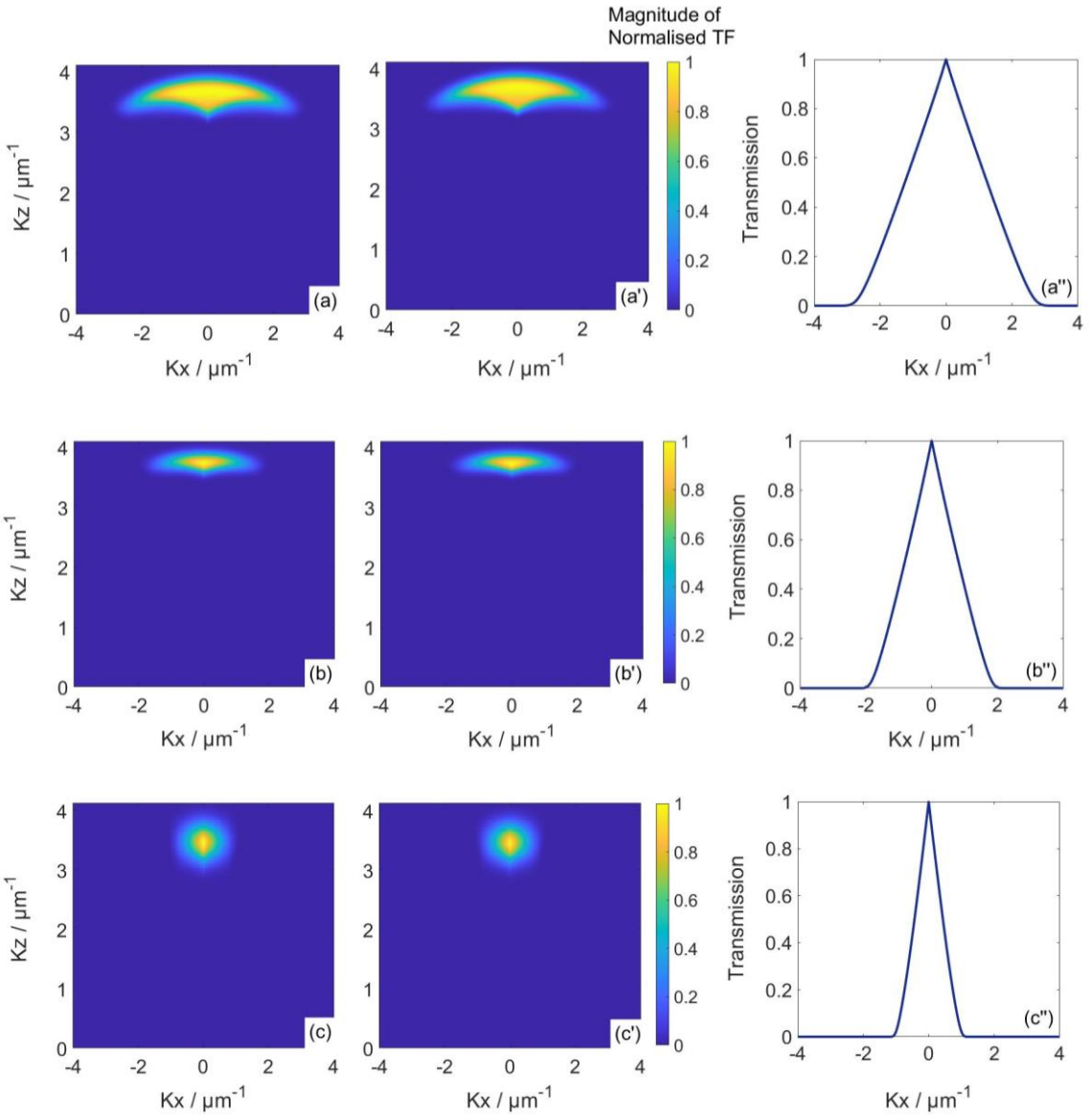

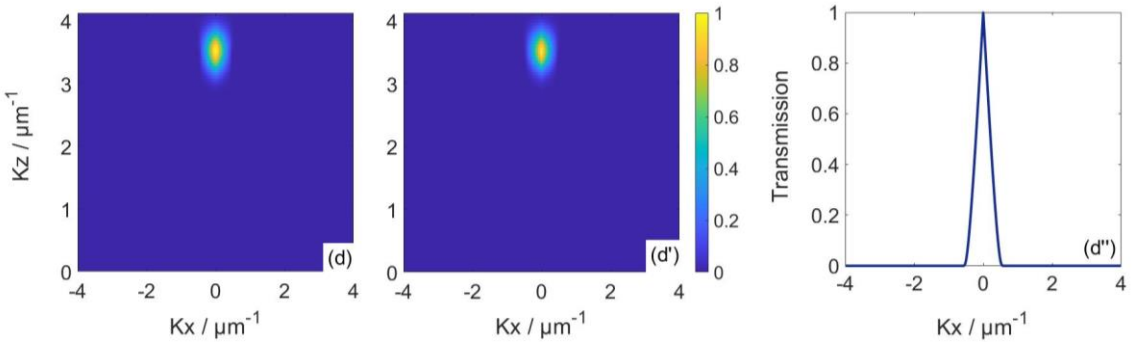

Figure 3. Simulated TFs of the EFO, UFO and foil models. The 3D TF of (a to d) the foil and (a' to d') UFO models, and (a" to d") the 2D TF in the EFO model for the NA of (a to a") 0.8, (b to b") 0.55, (c to c") 0.3 and (d to d") 0.15. All the TFs are simulated considering a Gaussian light source with a mean wavelength of 0.57 μm, an FWHM bandwidth of 0.08 μm and an objective lens that obeys Abbe's sine condition.

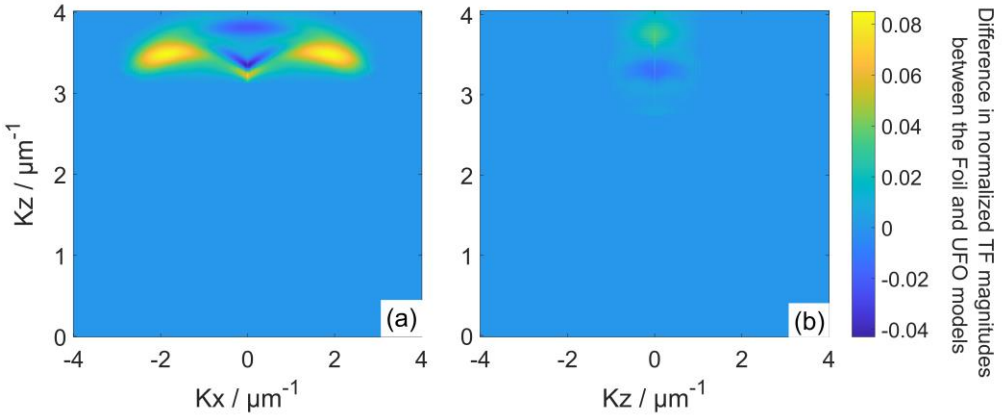

Figure 4. Difference between the magnitude of the normalized TFs in the foil and UFO models for the NA of (a) 0.8 and (b) 0.3.

5 Implications for CSI

All the models predict that there is the potential for errors attributable to the imaging of interference fringes through the optical system, even under ideal conditions with diffraction-limited optics. As has been well established in the literature, for the linear instrument response in

interferometry, all possible diffracted light needs to be captured by the objective lens, necessitating a sufficiently large NA for the optical instrument. This ensures the inclusion of the higher diffraction orders from steep slopes on smooth, continuous surfaces while limiting surface discontinuities (abrupt changes within a resolution cell) to less than a certain height (i.e., $\leq \lambda/4$)[43]. Predictions of residual nonlinear behavior for phase-based measurements can be calculated with any one of the three models compared in this paper, as a function of surface slope, surface height range, and optical configuration. This capability is one of the principal practical benefits of theoretical modeling, providing a way to optimise measurement configurations for the best results.

6 When to use a 3D model in place of a 2D model

As we have seen, all models should yield the same results for topography measurements based on the interference phase, assuming negligible polarization effects. This raises the question of where the models differ, and specifically, when a 2D model such as the EFO approach is no longer adequate for predicting measurement results and a 3D model is necessary.

The key difference between 2D and 3D approaches becomes apparent if we calculate surface profile using the shape of the interference fringes rather than the mean phase at the plane that intersects the object surface. The FDA-envelope analysis method is one such approach to topography measurement that is influenced by the shape of the interference pattern, particularly at high NA, when focus effects become significant. The disparity between the reconstructed profiles using 2D and 3D TFs at high NA is illustrated in the example presented in Figure 5, which shows the predicted measurement error for tests S1, S4 and S5. The EFO model uses the

obliquity factor that is equivalent to averaging the frequency projections along the vertical axis, enabling the application of a linear 2D TF. While Figure 2 indicates that the FDA-phase provides nearly identical results for all models, this simplification lacks details about the variation in possible K_z values as a function of K_x, as presented in the 3D TFs in the foil and UFO models.

Although this approximation is acceptable at low NA values, it proves inadequate at high NAs. For high NAs (above 0.2), the obliquity factor approximation fails to accurately represent the shape of the interference signal, and consequently, the reconstructed profile. Figure 5 illustrates the height error obtained by the foil, UFO and foil models using the same FDA-envelope analysis. As shown in Figure 5, the 3D foil and UFO models yield nearly identical results. However, the 2D EFO model underestimates the measurement error as the NA increases. Importantly, this discrepancy does not improve in the limit of small surface heights for coherence-based measurements—the EFO model is not up to the task of correctly predicting the shape of the interference fringes at high NA, even for nominally flat surfaces[20].

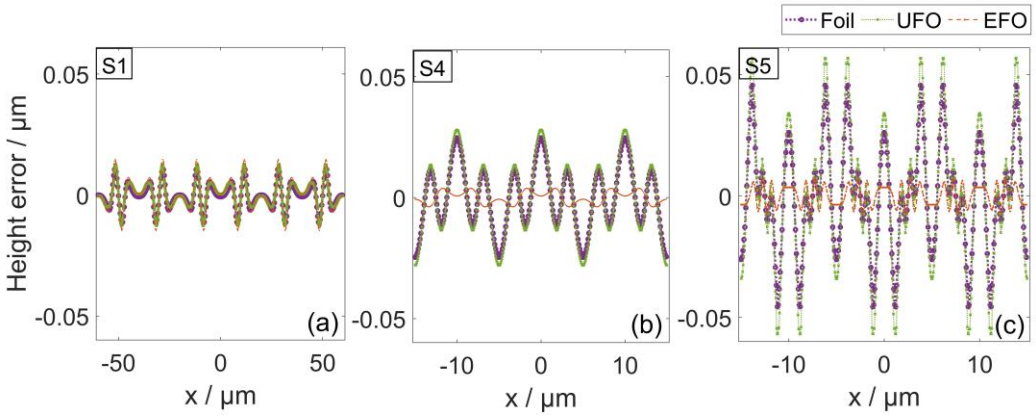

Figure 5. Difference between the reconstructed and nominal profiles for EFO, UFO and foil models associated with (a) S1, (b) S4 and (c) S5 tests. Reconstructed profiles are obtained using the same FDA-envelope analysis for all models.

7 Conclusion

Due to the wide range of CSI applications, the development of physics-based models to predict interference signals and analyse measurement results is of great interest. Despite the limitations of the approximate models, they can provide a powerful means for CSI modelling using basic scalar diffraction and linear imaging theory. The EFO, UFO and foil models are approximate models based on scalar diffraction theory. These models benefit from the linear nature of their imaging theories, so that the transfer characteristic of a CSI instrument can be defined by a linear filtering operation.

In the foil model, the 3D object is defined as a thin foil-like model, and the 3D surface TF is calculated by numerical integration. The EFO method simplifies the surface topography to a phase object at a constant equivalent wavelength and uses an analytical form for the 2D partially-coherent optical TF to map the object field to the image field in the spatial frequency domain. In a similar manner to the EFO model, the UFO approach treats the object as a phase object, but preserves the effects of multiple illumination incident angles, and relies on an analytical 3D optical TF to calculate the interference signal.

In this paper, we demonstrate the degree of agreement for these three approximate scaler diffraction and imaging models using software simulations. The RMS of the difference between the simulated profiles obtained by each two models is within the sub-nanometre range. The cross-sectional view of the UFO and foil 3D TFs in the *xz*-plane and the 2D TF of EFO along the *x*-axis are in good agreement, so that the average of the RMS of the difference between the magnitude of the normalised TFs of the UFO and foil models over the provided range of NAs is of the order of 10^{-3}. The EFO, UFO and foil models applied to various 2D profiles, including

sinusoids, step and rectangular surface features, for different instrument configurations illustrate the applicability of these methods for piecewise-continuous, relatively smooth surfaces.

In future work, we intend to compare the simulated profiles obtained by these models with a more comprehensive range of profiles, including various slope angles and curvatures within their validity range. Furthermore, to verify the measurement results, we will compare the results of these theoretical predictions with the experimental results.

Acknowledgements

This work was supported by the European Metrology Programme for Innovation and Research (EMPIR) project [TracOptic, 20IND07]. Helia Hooshmand was supported by the European Union [ERC, AI-SURF, 101054454] and would also like to thank the UKRI Research England Development (RED) Fund for supporting this work via the Midlands Centre for Data-Driven Metrology. Rong Su is grateful for the support from the National Natural Science Foundation of China [62105204, 52335010].

Code, Data and Materials Availability

Derived data supporting the findings of this study are available from the corresponding author on request.

References

1. J. Schmit and A. Pakuła, "White Light Interferometry," in *Handbook of Advanced Nondestructive Evaluation*, N. Ida and N. Meyendorf, Ed., pp. 421-467, Springer International Publishing, Cham (2019).
2. R. K. Leach, *Advances in Optical Surface Texture Metrology*, IOP Publishing, London (2020).
3. T. Yoshizawa, *Handbook of Optical Metrology: Principles and Applications*, CRC Press, New York (2017).
4. M. Thomas, R. Su, N. Nikolaev, J. Coupland and R. K. Leach, "Modeling of interference microscopy beyond the linear regime," *Opt. Eng.* **59**(3), 034110 (2020)
5. T. Pahl, S. Hagemeier, M. Künne, D. Yang and P. Lehmann, "3D modeling of coherence scanning interferometry on 2D surfaces using FEM," *Opt. Express* **28**(26), 39807-39826 (2020)
6. W. Xie, P. Lehmann, J. Niehues and S. Tereschenko, "Signal modeling in low coherence interference microscopy on example of rectangular grating," *Opt. Express* **24**(13), 14283-14300 (2016)
7. P. de Groot and X. Colonna de Lega, "Signal modeling for low-coherence height-scanning interference microscopy," *Appl. Opt.* **43**(25), 4821-4830 (2004)
8. E. Wolf, "Three-dimensional structure determination of semi-transparent objects from holographic data," *Opt. Commun.* **1**(4), 153-156 (1969)
9. N. Streibl, "Three-dimensional imaging by a microscope," *J. Opt. Soc. Am. A* **2**(2), 121-127 (1985)
10. J. Goodman, *Introduction to Fourier Optics*, Macmillan Learning, New York (2017).

11. P. Beckmann and A. Spizzichino, *The Scattering of Electromagnetic Waves from Rough Surfaces*, Artech House, Norwood, MA (1987).
12. J. A. Ogilvy, *Theory of Wave Scattering From Random Rough Surfaces*, Taylor & Francis, New York (1991).
13. M. Born and E. Wolf, *Principles of Optics: Electromagnetic Theory of Propagation, Interference and Diffraction of Light*, Elsevier Science, United Kingdom (2013).
14. M. Roy, I. Cooper, P. Moore, C. J. R. Sheppard and P. Hariharan, "White-light interference microscopy: effects of multiple reflections within a surface film," *Opt. Express* **13**(1), 164-170 (2005)
15. J. M. Coupland and J. Lobera, "Holography, tomography and 3D microscopy as linear filtering operations," *Meas. Sci. Technol.* **19**(7), 074012 (2008)
16. J. Coupland, R. Mandal, K. Palodhi and R. K. Leach, "Coherence scanning interferometry: linear theory of surface measurement," *Appl. Opt.* **52**(16), 3662-3670 (2013)
17. R. Mandal, J. Coupland, R. K. Leach and D. Mansfield, "Coherence scanning interferometry: measurement and correction of three-dimensional transfer and point-spread characteristics," *Applied Optics* **53**(8), 1554-1563 (2014)
18. C. J. R. Sheppard, "Imaging of random surfaces and inverse scattering in the Kirchoff approximation," *Waves in Random Media* **8**(1), 53-66 (1998)
19. P. J. de Groot and X. Colonna de Lega, "Fourier optics modeling of interference microscopes," *J. Opt. Soc. Am. A* **37**(9), B1-B10 (2020)
20. P. de Groot, X. C. de Lega, R. Su, J. Coupland and R. K. Leach, "Modeling of coherence scanning interferometry using classical Fourier optics," *Opt. Eng.* **60**(10), 1-19 (2021)
21. P. Lehmann, M. Künne and T. Pahl, "Analysis of interference microscopy in the spatial frequency domain," *J. Phys. Photon.* **3**(1), 014006 (2021)

22. P. Lehmann, T. Pahl and J. Riebeling, "Universal Fourier optics model for virtual coherence scanning interferometers," *Proc. SPIE*, **12619**, 126190O (2023)
23. R. Su, J. Coupland, C. Sheppard and R. K. Leach, "Scattering and three-dimensional imaging in surface topography measuring interference microscopy," *J. Opt. Soc. Am. A* **38**(2), A27-A42 (2021)
24. P. de Groot and X. Colonna de Lega, "Fourier optics modelling of instrument response for interference microscopy," *Proc. SPIE*, **11490**, 114900T (2020)
25. P. J. de Groot, "The instrument transfer function for optical measurements of surface topography," *J. Phys. Photon.* **3**(2), 024004 (2021)
26. R. Su and R. K. Leach, "Physics-based virtual coherence scanning interferometer for surface measurement," *Light: Advanced Manufacturing* **2**(2), 120 - 135 (2021)
27. R. Su, Y. Wang, J. Coupland and R. K. Leach, "On tilt and curvature dependent errors and the calibration of coherence scanning interferometry," *Opt. Express* **25**(4), 3297-3310 (2017)
28. R. Su, M. Thomas, M. Liu, J. Drs, Y. Bellouard, C. Pruss, J. Coupland and R. K. Leach, "Lens aberration compensation in interference microscopy," *Opt. Lasers Eng.* **128**(128), 106015 (2020)
29. N. Nikolaev, J. Petzing and J. Coupland, "Focus variation microscope: linear theory and surface tilt sensitivity," *Appl. Opt.* **55**(13), 3555-3565 (2016)
30. H. Hooshmand, T. Pahl, P. de Groot, P. Lehmann, A. Pappas, R. Su, R. K. Leach and S. Piano, "Comparison of approximate methods for modelling coherence scanning interferometry," *Proc. SPIE*, **12619**, 126190R (2023)
31. P. Lehmann, S. Hagemeier and T. Pahl, "Three-Dimensional Transfer Functions of Interference Microscopes," *Metrology* **1**(2), 122-141 (2021)
32. M. Totzeck, "Numerical simulation of high-NA quantitative polarization microscopy and corresponding near-fields," *Optik* **112**(9), 399-406 (2001)

441 33. C. J. R. Sheppard and K. G. Larkin, "Effect of numerical aperture on interference fringe spacing,"
442 *Appl. Opt.* **34**(22), 4731-4734 (1995)
443 34. P. Lehmann, L. Hüser, A. Stelter and T. Kusserow, "Lateral resolution enhanced interference
444 microscopy using virtual annular apertures," *J. Phys. Photon.* **5**(1), 015001 (2023)
445 35. P. Lehmann and T. Pahl, "Three-dimensional transfer function of optical microscopes in reflection
446 mode," *J. Microsc.* **284**(1), 45-55 (2021)
447 36. C. J. R. Sheppard, M. Gu and X. Q. Mao, "Three-dimensional coherent transfer function in a
448 reflection-mode confocal scanning microscope," *Opt. Commun.* **81**(5), 281-284 (1991)
449 37. K. G. Larkin, "Efficient nonlinear algorithm for envelope detection in white light interferometry," *J.*
450 *Opt. Soc. Am. A* **13**(4), 832-843 (1996)
451 38. P. de Groot and L. Deck, "surface profiling by analysis of white-light interferograms in the spatial
452 frequency domain," *J. Mod. Opt.* **42**(2), 389-401 (1995)
453 39. I. Kiselev, E. I. Kiselev, M. Drexel and M. Hauptmannl, "Noise robustness of interferometric surface
454 topography evaluation methods. Correlogram correlation," *Surf. Topogr.: Metrol. Prop.* **5**(4), 045008
455 (2017)
456 40. A. Harasaki and J. C. Wyant, "Fringe modulation skewing effect in white-light vertical scanning
457 interferometry," *Appl. Opt.* **39**(13), 2101-2106 (2000)
458 41. L. Xin, J. Dou, Z. Yang and Z. Liu, "Composite wavelet decomposition algorithm combined with
459 correlation analysis in white-light scanning interferometry," *Results Phys.* **40**(105870 (2022)
460 42. E. Hecht, *Optics*, Addison-Wesley, United Kingdom (1998).
461 43. P. de Groot, X. Colonna de Lega, R. Su and R. K. Leach, "Does interferometry work? A critical look
462 at the foundations of interferometric surface topography measurement," *Proc. SPIE*, **11102**, 111020G
463 (2019)
464

Caption List

Figure 1. The interference fringe pattern simulated by (a) EFO, (b) UFO and (c) foil corresponding to the S1 test in Table 1.

Figure 2. (a to i) Nominal and simulated profiles obtained by the EFO, UFO and foil models along the *x*-axis. The specification of the samples and optics used at each row are provided in Table 1. (a' to i') difference between the simulated and nominal profiles for EFO, UFO and foil models. (a" to i") relative signal strength of the fringe data in the EFO, UFO and foil models.

Figure 3. Simulated TFs of the EFO, UFO and foil models. The 3D TF of (a to d) the foil and (a' to d') UFO models, and (a" to d") the 2D TF in the EFO model for the NA of (a to a") 0.8, (b to b") 0.55, (c to c") 0.3 and (d to d") 0.15. All the TFs are simulated considering a Gaussian light source with a mean wavelength of 0.57 μm, an FWHM bandwidth of 0.08 μm and an objective lens that obeys Abbe's sine condition.

Figure 4. Difference between the magnitude of the normalized TFs in the foil and UFO models for the NA of (a) 0.8 and (b) 0.3.

Figure 5. Difference between the reconstructed and nominal profiles for EFO, UFO and foil models associated with (a) S1, (b) S4 and (c) S5 tests. Reconstructed profiles are obtained using the same FDA-envelope analysis for all models.

Table 1. Summary of simulated samples and optics. The mean wavelength equals 0.57 μm for all simulations.